Advanced Composites and Hybrid Materials (2025) 8:131
https://doi.org/10.1007/s42114-025-01227-y

RESEARCH

Intranasal delivery of metformin using metal–organic framework (MOF)-74-Mg nanocarriers

Muzhaozi Yuan[1] · Zongsu Han[2] · Yogish Somayaji[3] · Nguyen Nguyen[1] · Hanwen Hu[1] · Leelavathi N. Madhu[3] · Sahithi Attaluri[3] · Maheedhar Kodali[3] · Yihao Yang[2] · Yu-Chuan Hsu[2] · Avik Ahuja[1] · Rahul Srinivasan[4,5] · Jean-Philippe Pellois[6] · Hong-Cai Zhou[2] · Ashok K. Shetty[3,5] · Ya Wang[1,7,8]

Received: 15 July 2024 / Revised: 10 December 2024 / Accepted: 8 January 2025

Abstract

Dosage tolerance is one of the translational challenges of using metformin (Met) in brain therapeutics. This paper presents metal–organic framework (MOF)-74-Mg nanocarriers (NCs) for intranasal (IN) delivery of brain-specific agents with a prolonged release time. We confirmed their excellent biocompatibility (5 mg/mL) and intrinsic fluorescence properties (370/500 nm excitation/emission peak) in Neuro-2A cells. This NC exhibited a high Met loading rate (10% wt/wt) and a sustained and prolonged release pattern of Met (90% release in 16 h) in Dulbecco's Modified Eagle Medium. We observed an optimal brain accumulation of Met-MOF (9% of the injected dosage) 8 h after IN injection. This percentage is at least 82 times higher than oral administration. Confocal imaging demonstrated significantly higher uptake of Met-MOF, 45 min after IN injection, by 79–85% neurons and 93–97% microglia than astrocytes and oligodendrocytes across 5xFAD mouse brain regions, including hippocampus and striatum. These results suggest MOF-74-Mg is a potential NC for high brain Met accumulation, real-time imaging, and prolonged and sustained release of Met and other neurotherapeutic agents that are challenging to deliver using traditional carriers and administration routes.

Keywords Metal–organic framework · Metformin · Sustained drug release · Intranasal administration · Neuron · Microglia

1 Introduction

Both clinical and preclinical studies have suggested metformin (Met), commonly used for type 2 diabetes, holds high potential as a repurposing drug for treating Alzheimer's disease (AD) [1] and Parkinson's disease (PD) [2]. Preclinical studies have demonstrated that Met mitigates

Muzhaozi Yuan, Zongsu Han, Yogish Somayaji, and Nguyen Nguyen are co-first authors.

Ashok K. Shetty and Ya Wang are co-senior authors.

✉ Muzhaozi Yuan
muzhaozi.yuan@tamu.edu

✉ Zongsu Han
zongsu-han@tamu.edu

✉ Ya Wang
ya.wang@tamu.edu

[1] J. Mike Walker '66 Department of Mechanical Engineering, Texas A&M University, College Station, TX 77843, USA

[2] Department of Chemistry, Texas A&M University, College Station, TX 77843, USA

[3] Institute for Regenerative Medicine, Department of Cell Biology and Genetics, College of Medicine, Texas A&M University, College Station, TX 77843, USA

[4] Department of Neuroscience & Experimental Therapeutics, College of Medicine, Texas A&M University, 8447 Riverside Pkwy, Bryan, TX 77807, USA

[5] Texas A&M Institute for Neuroscience (TAMIN), Texas A&M University, College Station, TX 77843, USA

[6] Department of Biochemistry and Biophysics, Texas A&M University, College Station, TX 77843, USA

[7] Department of Electrical and Computer Engineering, Texas A&M University, College Station, TX 77843, USA

[8] Department of Biomedical Engineering, Texas A&M University, College Station, TX 77843, USA

Published online: 18 January 2025

hallmark features of AD pathology, including the reduced accumulation of amyloid plaque deposition, inhibited tau hyperphosphorylation, and improved memory deficits in AD mice [1]. However, it is noteworthy that the effects of Met on cognitive performance can be age-dependent: it enhances executive functions and learning speed in young and middle-aged mice, while chronic administration in older AD mice (17 months) has been associated with cognitive impairments [3]. Met has shown neuroprotective effects against dopaminergic (DA) neuron loss in PD models, a hallmark of PD pathology [2]. These protective effects are attributed to its regulation of mitochondrial function, which reduces the generation of reactive oxygen species (ROS). Met also attenuates neuroinflammation by suppressing microglial activation [2].

Additionally, preclinical studies suggest that Met enhances autophagy and directly binds to alpha-synuclein, preventing its aggregation and further supporting its therapeutic potential. One of the main mechanisms of Met for neuroprotection is the activation of AMP-activated protein kinase (AMPK) activity, which improves mitochondria dysfunction to reduce ROS generation, modulates microglia activation to suppress neuroinflammation, and upregulates autophagy [4]. The effects on mitochondria are supported by findings in nematode *C. elegans*, where Met at a concentration of 50 μM improves neuronal viability by restoring mitochondrial respiration activities via inhibition of mitochondrial complex I [5]. Met treatment also mediates anti-inflammatory effects via reducing microglia clustering and enabling microglia conversion from M1 phenotype into a non-inflammatory M2 phenotype, through AMPK pathway [6, 7], along with the reduction of proinflammatory cytokines, such as IL-1β, IL-6, and TNF-α, in microglia [8].

Currently, there is an ongoing clinical trial (NCT05781711) investigating the efficacy of Met in PD patients. Despite the promising potential, delivering a therapeutic quantity to the brain remains challenging. A recent clinical trial (NCT00620191) demonstrated the beneficial effect of Met on cognitive function in patients with amnestic mild cognitive impairment [9]. However, only 32.5% of patients could tolerate the highest dose from oral administration (1500 mg/day). The causes are multitudes: the short half-life (2–6 h) [4], the slow and incomplete absorption by the gastrointestinal tract [10], and the low percentage penetration into the cerebrospinal fluid (CSF) [11]. To address this, long-acting Met (Glucophage® XR) forms are tested in an ongoing clinical trial (NCT04098666). Although they offer a slower absorption rate and an increased time to reach maximum plasma concentration compared to the previous short-acting version (7 v.s. 3 h) [12], limitations persist due to the potential side effects at high doses by oral administration, such as vitamin B_{12} deficiency [13] and gastrointestinal adverse effects [4]. Overcoming challenges related to effective drug delivery remains critical for successful translation to clinical use.

Thus, there is an urgent need to develop a nanocarrier (NC) for Met and many other neurotherapeutic drugs, genes [14], and peptides [15] that are challenging to deliver using traditional carriers or injection routes. Conventional routes for treating AD and PD, such as intravenous injection (IV) or oral administration, often face limitations due to barriers to reaching the brain, including the blood–brain barrier (BBB), resulting in low brain accumulation [16], demonstrated by animal models and different type of NCs [17, 18]. In contrast, intranasal (IN) delivery, based on the olfactory nerve-to-brain and trigeminal nerve pathways, offers a noninvasive method facilitating direct entry into the brain without BBB penetration [19]. This allows for direct and efficient drug transport from the nasal cavity to the brain, enabling precise targeting with minimal systemic circulation and reducing the risk of systemic side effects and toxicity [20]. However, the efficacy of IN delivery varies depending on the drug and nanoparticle (NP) types, as the uptake mechanism remains poorly understood [19]. For polymeric NPs, IN delivery can increase their accumulation in brain tissue from 0.077% (IV case) to 0.387% (a fivefold increase) of the injected dose at 12 h [21]. For drug nanoemulsion systems, IN delivery can enhance drug concentration in the brain by 42 times compared to IV delivery [22]. Similarly, for another nanoemulsion system of cyclosporine A, IN delivery results in a 37-fold higher brain concentration than IV delivery [23]. Additionally, IN administration of oxytocin showed higher CSF concentrations than IV administration [24]. Many other factors can also affect the cell uptake ability of NCs, such as size, shape, and surface functions [25]. Notably, it is reported that rod-shaped NCs have more efficient diffusion than spheres, including enhanced cellular absorption and mucosal penetration [26]. Further effort is needed to explore the IN delivery of Met-loaded NCs. In addition, it is essential to examine the neuron and microglia targeting of IN-delivered NC for Met due to the crucial role of neuron and microglia functionality in AD pathology. Specifically, as the central nervous system (CNS)'s primary immune cells, microglia are a promising target for AD due to their role in neuroinflammation [27]. The activation of microglia is triggered by the mitochondrial complex I activity, which drives the production of ROS [28]. As a repurposing drug, MET shows its inhibition of mitochondrial complex I and modulation of the inflammatory processes via AMPK-independent and AMPK-dependent pathways [4]. Met also mitigates the dysfunction of microglial autophagy and increases the presence of microglia around Aβ plaques, resulting in enhanced Aβ clearance [29]. In addition, Met acts on neurons by attenuating neuronal apoptosis by inhibiting ROS production [1]. However, therapeutic reports on the effects of Met on astrocytes and oligodendrocytes are limited [29]. Considering the

unique impact of Met on microglia and neurons, developing NCs for Met that preferably target neurons and microglia offers the potential for modulating neuronal activities and microglial activation, addressing multiple disease mechanisms for neuroprotection.

Nanosized biocompatible metal–organic frameworks (MOFs) are promising candidates for Met delivery due to their high-loading capacity of various hydrophobic and hydrophilic drugs, along with tunable and controlled drug release properties [30], thanks to their high porosity [31] and customizable pore functionality [32]. Popular MOF-based carriers like (Fe)ZIF-8@alginate [33] and (Fe)MIL-100@alginate [34] can release 90% of Met for up to 8 h, but both systems are detrimental to brain health due to Fe ion [35]. Also, the Met payload is relatively low: 7.2 wt% and 6.68 wt% for (Fe)MIL-100@alginate and (Fe)ZIF-8@alginate, respectively. Other Met carriers, such as nanoerythrosomes, show high biocompatibility and an extended-release time longer than 30 h but have a limited Met loading rate (1.66 wt%) and lack in vivo brain delivery demonstration [36]. Moreover, polymeric carriers in the micro range lack sustained release (56% of Met released in the first 2 h) [37]. Thus, there is an unmet need for brain-targeting delivery of Met using size-suitable NCs with high biocompatibility and loading capacity.

MOF-74, with 1D hexagonal channels [38] and chelating coordination of carboxyl and hydroxyl groups, is one of the most promising candidates with excellent tunability and stability [39]. MOF-74-Mg has successfully encapsulated various drugs with different solubilities and molecular sizes [40]. Mg^{2+} at 4.0 mM shows potential neuroprotective effects on DA neurons in a 1-methyl-4-phenylpyridinium (MPP +) induced in vitro model of PD [41]. The number of DA neurons is well maintained without loss, and the neurite length is preserved and ameliorated by adding Mg^{2+} after MPP + -induced toxicity. Compared to other ions commonly used in the MOF-74 nanostructures, such as Zn^{2+}, Co^{2+}, and Cu^{2+}, with demonstrated neurotoxicity [42, 43], Mg^{2+} emerges as the most suitable choice as a MOF component for brain-related applications.

In addition to its potential as an NC, MOF-74 exhibits intrinsic fluorescence properties [44] due to the interaction between solvent molecules and its π-conjugated organic linker [45]. This property enables real-time tracking and imaging of biodistribution and tissue targeting without additional fluorescence dyes, reducing system complexity in the biomedical field. Studies show that trace amounts of H_2O can enhance the fluorescence of MOF-74-Zn at 100 nm by disrupting coordination bonding between the oxygen atom of the organic linker and Zn^{2+} ions and forming hydrogen bonding between the oxygen atom of the organic linker and the H_2O molecule, thus altering electron distribution [45]. Studies also show that in MOF-74-Cu with a micro-sized sheet-like shape, a high-intensity fluorescence between 400 and 650 nm was observed when excited at 360 nm [46]. However, the neurotoxicity of metal ions in these structures limits their suitability for brain-related drug delivery. Zn^{2+} at the concentration of 10 ppm in drinking water increases spatial memory impairment in Tg2576 mice [42]. Cu^{2+} at the concentration of 10 μM causes the ROS production of PC-12 cells after 3 h of incubation [47]. Notably, no report has been made on using MOF-74-Mg for fluorescence imaging in bio-applications, which could offer a more neuro-friendly option than other nanosized counterparts.

To further address the abovementioned issues, we first synthesized and characterized the MOF-74-Mg structure as an NC for Met in this study and investigated its drug-loading capacity and release kinetics in a cell-free medium, as shown in Fig. 1a. We then assessed the effects of Met-loaded MOF-74-Mg against H_2O_2-induced toxicity in Neuro-2A cells while examining the self-fluorescence of MOF-74-Mg in the same cell line, as illustrated in Fig. 1b. To enhance the fluorescence of MOF-74-Mg in living animals, Met-loaded MOF-74-Mg was further modified with a fluorescence dye, Cyanine3 (Cy3). Importantly, we delivered Met-loaded MOF-74-Mg to the brain through IN administration, as depicted in Fig. 1c. Then, we examined their interactions with neurons, microglia, astrocytes, and oligodendrocytes using confocal microscopy and quantified the presence of MOF-74-Mg across multiple brain regions using Inductively Coupled Plasma Mass Spectrometer (ICP-MS) as illustrated in Fig. 1d.

2 Experimental

2.1 Materials

All reagents were commercially available and used without further purification.

2.2 Preparation of MOF-74-Mg NC

The synthesis method for nano-scaled MOF-74-Mg is a modification of the literature [48]. 2,5-dihydroxyterphthalic acid (1.0 mmol, 0.20 g) was added to 5 mL of *N*-dimethylformamide (DMF). The mixture was then added to 8 mL of DMF solution containing Mg $(NO_3)_2 \cdot 6H_2O$ (2.6 mmol, 0.67 g) under continuous stirring for 24 h. The powder was collected by centrifugation, washed with fresh DMF, and dried in air. The obtained samples were used in the following study without further modifications.

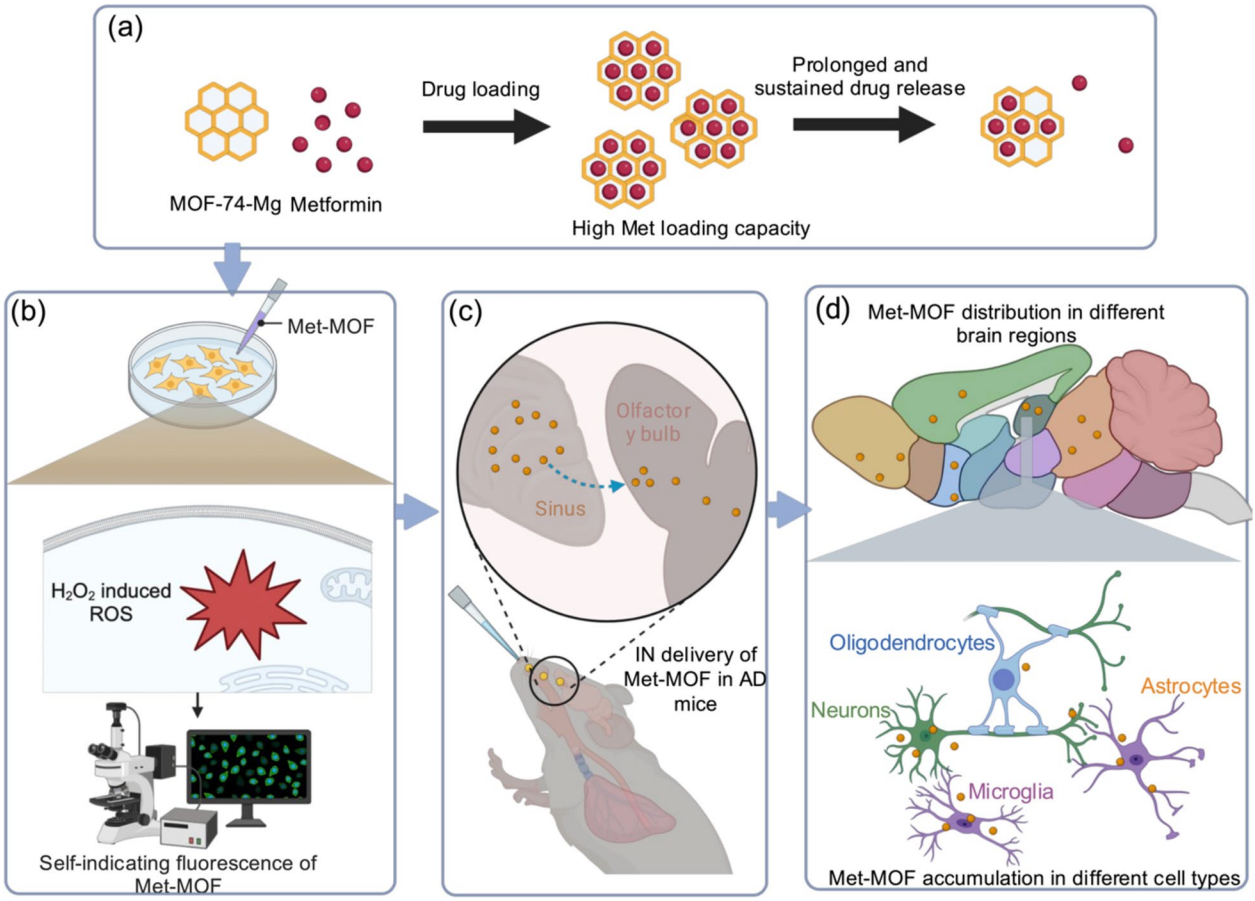

Fig. 1 Schematic illustration of brain targeting of nanosized MOF-74-Mg through IN delivery: **a** Drug loading and release characteristics of MOF-74-Mg for Met are evaluated. **b** The impact of Met-loaded MOF-74-Mg in H_2O_2-induced toxicity in Neuro-2A cells and its self-fluorescence is explored. **c** The Met-loaded MOF-74-Mg is targeted to the mouse brain through IN delivery. The olfactory nerve-to-brain pathway allows a direct route for transporting Met-loaded MOF-74-Mg from the nasal system to different brain areas. **d** The presence of MOF-74-Mg across multiple brain regions is quantified, and their interactions with neurons, microglia, astrocytes, and oligodendrocytes are revealed using confocal microscopy

2.3 Characterization

Scanning electron microscopy (SEM) images for all samples were taken and recorded on a FEI Quanta 600 Fe-SEM scanning electron microscope. The size distribution of MOF-74-Mg was analyzed based on at least 100 NCs using ImageJ software. Powder X-ray Diffraction (PXRD) patterns were collected on a Bruker-AXS D8 Vario X-ray powder diffractometer. Zeta potential and hydrodynamic diameter of MOF-74-Mg were measured on a Malvern Zetasizer Nano ZS equipment (Malvern Instruments Inc.). Triplicated experiments were performed to obtain the average value.

2.4 Fluorescent test

The fluorescence excitation and emission spectra and the quantum yield measurement of the NCs were recorded respectively at a Horiba spectrofluorometer instrument. All fluorescence analysis experiments were tested under the experimental conditions of an excitation wavelength of 370 nm.

2.5 Loading efficiency of Met

For the loading of Met into MOF-74-Mg, about 1.3 g MOF-74-Mg was added to a methanol solution that contained 300 mg Met. The mixture was kept for 3 days. Then, the samples were separated through centrifugation and washed 3 times with fresh methanol to make sure the Met molecules at the surface of MOF-74-Mg were washed away and weighed.

The UV–Vis absorption spectra of Met in the supernatant fluid were measured using a Shimadzu UV-2450 spectrophotometer (Shimadzu Corp.). The absorption spectra of the standard Met solutions in methanol were measured to obtain a standard curve for calculating Met concentration in the supernatant fluid. The loading efficiency (LE) after 72 h

and the payload of Met into MOF-74-Mg were calculated according to the following equations:

$$LE\ (\%) = \frac{Total\ added\ Met - unloaded\ Met\ in\ the\ supernatant\ fluid}{Total\ added\ Met} \times 100\% \quad (1)$$

$$Payload = \frac{Mass\ of\ Met\ loaded\ by\ \mathrm{MOF}}{mass\ of\ \mathrm{MOF}} \quad (2)$$

2.6 Release profile of Met in cell-free medium

For the release profile of Met, 5 mg of Met-loaded MOF-74-Mg samples was suspended in 5 mL of Dulbecco's Modified Eagle Medium (DMEM) at 37 °C in each tube. Every 10 min, the UV–Vis absorption spectra of the supernatant fluid were measured and recorded using a Shimadzu UV-2450 spectrophotometer (Shimadzu Corp.) at 235 nm. The absorption spectra of the standard Met solutions in DMEM medium were also measured to obtain the standard curve for calculating Met concentration in the supernatant fluid.

2.7 *Cell viability and H_2O_2-induced toxicity evaluation*

Neuro-2A cells were seeded into a 48-well plate and cultured for 1 day. The cells were then incubated with Met-loaded MOF-74-Mg at different concentrations for different periods with and without the co-treatment of H_2O_2. After each incubation period, the cells were harvested by detaching them with 0.25% trypsin–EDTA and neutralizing them in DMEM. The cell suspension was then centrifuged, and the supernatant was discarded. The cells were stained with SYTOX Green and SYTO 59 Red for flow cytometric analysis. The staining solutions were diluted at 1:2000 for SYTOX Green and 1:1000 for SYTO 59 Red for 30 min in the dark. Cell viability was measured using a BD Accuri C6 flow cytometer equipped with FL 1 detector (553 nm) and FL 4 detector (675 nm) (Event number > 10,000).

2.8 In vitro *fluorescence imaging*

Neuro-2A cells were seeded into a 12-well plate and cultured for 1 day. The cells were then incubated with Met-loaded MOF-74-Mg at 2.58 mg/mL concentrations for 2, 4, 8, and 12 h. Neuro-2A cells were washed with phosphate-buffered saline (PBS) following NC incubation to eliminate residual NCs and unbound dyes. Subsequently, a working SyTO 59 fluorescent dye solution was prepared to stain all Neuro-2A cells comprehensively. The cells were then incubated with the fluorescent dye for 10 min at room temperature in the dark, ensuring optimal staining conditions. A second PBS wash was performed to remove excess dyes and unbound NCs, enhancing the specificity of the fluorescent signal. The stained cells were imaged on an EVOS M7000 Imaging System (Invitrogen) using a × 20 objective. Filter cubes for fluorescence microscopy included GFP ($\lambda_{ex}/\lambda_{em}$ = 459–481/500–550 nm) and RFP ($\lambda_{ex}/\lambda_{em}$ = 511–551/573–613 nm). Subsequent image analysis was conducted using dedicated software to quantitatively assess and analyze the fluorescent signal within the Neuro-2A cells, providing a comprehensive understanding of Met-MOF NC-cell interactions.

2.9 Animal study

2.9.1 Animals

Three-month-old male AD mice (5xFAD-tg mice B6SJL strain) and wild-type C57BL6 mice purchased from Jackson Laboratories (Cat No: 100012-JAX) were employed in this study. These mice were bred in-house and kept at Texas A&M University's vivarium. Animals were maintained in a climate-controlled room with a 12:12-h light–dark cycle and free access to food and water. The Animal Care and Use Committee at Texas A&M University approved all experimental procedures performed in this study.

2.9.2 Intranasal administration of Met-loaded MOF-74-Mg and determination of their brain concentration

Met-loaded MOF-74-Mg NCs were administered intranasally to wild-type mice (n = 3 for each time point: 8, 12, and 16 h). Both nostrils were utilized during IN administration. The nostrils of each mouse were treated first with 20 µL of hyaluronidase (H3506, Sigma-Aldrich) dissolved in a sterile PBS solution to increase the permeability of the nasal mucous membrane. After 30 min, each mouse was administered with Met-loaded MOF-74-Mg NCs at 400 uL containing 22 mg NCs.

The measurement of Mg^{2+} ions concentration by Inductively Coupled Plasma Mass Spectrometer (ICP-MS) was performed to reflect the concentration of MOF-74-Mg NCs. 8, 12, and 16 h after intranasal administration of Met-loaded MOF-74-Mg NCs, wild type mice (n = 3 for each time point) were intracardially perfused using 4% paraformaldehyde. The brain tissues from 4 brain regions: the hippocampus, cortex, midbrain, and cerebellum were collected. Brain tissue samples were then digested using acid. Briefly, 1 mL HNO_3 (65%) was added to each tissue sample and then heated to 80 °C overnight. Clear solutions were obtained after that. Then 0.2 mL of the solution was transferred out, and NaOH solution (0.256 mL) was added until the pH value reached 7. The

samples were then diluted into 2% nitric acid and tested on the PerkinElmer NexION 300D Inductively Coupled Plasma Mass Spectrometer (PerkinElmer, Inc.) for the concentrations of Mg^{2+} ions as a component of MOF-74-Mg NCs.

2.9.3 Measurement of Cy3-labeled Met-loaded MOF-74-Mg within neurons and microglia of AD mouse brain following intranasal administration

For Cy3 labeling, Met-loaded MOF-74-Mg were suspended in Cy3-dissolved methanol solutions for 24 h, followed by centrifuging and washing with methanol. The AD mice ($n=4$) were moderately anesthetized with ketamine, xylazine, and acepromazine. They were treated with 10 µl of hyaluronidase (Sigma-Aldrich, St. Louis, MO, USA) for each nostril to enhance the permeability of the nasal mucous membrane. Thirty minutes later, as detailed in our recent reports, Cy3-labeled Met-loaded MOF-74-Mg NCs were administered (5.5 mg particles in 200 µL of PBS/mouse) [49, 50]. The AD animals were euthanized 45 min after an intranasal administration of NCs. To visualize the labeled NCs and to quantify neurons and microglia containing these particles (green particles), serial sections from each animal were processed for single immunofluorescence staining of *neuronal nuclear protein* (NeuN) or ionized calcium-binding adaptor molecule 1 (IBA-1) to confirm the incorporation. Thirty micrometers thick serial (every 15th) sections through the forebrain and midbrain were used from each 5xFAD mouse ($n=4$/group) for NeuN or IBA-1 immunofluorescence staining. The primary antibodies comprised rabbit anti-NeuN (1:1000, Millipore Sigma) and goat anti-IBA-1 (1:1000, Abcam). Additionally, we also stained representative tissue sections for visualizing glial fibrillary acidic protein using rabbit anti-GFAP (1:3000 Agilent technologies) and oligodendrocytes using mouse anti-2′,3′-cyclic nucleotide-3′-phosphodiesterase (CNPase,1:500, Millipore) to understand the interaction of MOF-74-Mg with astrocytes and oligodendrocytes. The secondary antibodies employed in the study include donkey anti-rabbit IgG, donkey anti-goat IgG, or mouse anti-goat IgG tagged with Alexa Flour 594 (1:200, Invitrogen). Optical Z-stacks were sampled from different brain regions using a Nikon confocal microscope. For neurons and microglia, the quantitative analysis comprised images from three fields in every sampled subregion of the medial prefrontal cortex, hippocampal subregions (DG, CA1, and CA3), striatum, perirhinal cortex, and midbrain. MOF incorporation into neurons and microglia in these brain sections ($n=4$) was analyzed quantitatively.

2.10 Statistical analysis

Statistical analysis was performed using the *T*-test to assess the difference between the control group and the Met and MOF-treated groups. A *p*-value less than 0.05 was considered a significant difference.

3 Results and discussion

3.1 Characterization of MOF-74-Mg

The PXRD analyses confirmed the crystalline structure of MOF-74-Mg NCs, revealing typical diffraction peaks consistent with calculated data from the crystallographic structures and literature results [48] (Fig. 2a). PXRD patterns confirmed the delicate phase purities of the synthesized MOF-74-Mg. Also, as observed in the PXRD pattern comparison, Met loading did not alter the crystalline structure of MOF-74-Mg.

SEM images (Fig. 2b) depicted uniform short-rod-like morphology of as-synthesized MOF-74-Mg NCs before Met loading, with narrow size distribution (length: 135.3 ± 15.6 nm, diameter: 70.1 ± 7.3 nm). Post loading, MOF-74-Mg NCs retained similar shape and size, indicating unchanged morphologies. Rod-like elongated NPs, like those observed here, exhibit higher cellular affinity due to a larger surface area with a higher length/width ratio, facilitating enhanced cell membrane interactions and cellular internalization [51]. Due to reduced curvature-enhancing interactions with brain capillary endothelial cells, rod-like NPs possess superior BBB crossing ability and brain accumulation compared to spherical NPs [52]. It is also reported that rod-shaped NPs at 150×450 nm have better cellular absorption and mucosal penetrating capacity than spheres at 200 nm and thus can diffuse through mucus more efficiently [26]. The reason is likely due to the larger surface area/volume ratio, which enables stronger attachment with cell membranes.

The zeta potential of MOF-74-Mg, with and without Met-loading, was -15 ± 0.3 mV and -15 ± 1.0 mV, respectively, indicating unchanged surface charge post-loading. The hydrodynamic diameter of MOF-74-Mg and Met-loaded MOF-74-Mg was 169 ± 8 nm and 173 ± 7 nm, respectively, with a slight difference likely due to drug absorption. The difference between SEM-measured size and hydrodynamic diameter is worth noting, possibly due to NC accumulation.

Fluorescence properties of MOF-74-Mg were measured, showing maximum emission wavelength before and after Met and Cy3 loading at 430 nm, 500 nm, and 500/590 nm, respectively (Fig. 2c). The peak shift post-Met-loading suggests altered energy transfer. Cy3 loading induced a prominent peak at 590 nm, and the new energy transfer from the MOF to Cy3 induced intensity changes. The quantum yield of MOF-74-Mg, Met-loaded MOF-74-Mg, and Met&Cy3 loaded MOF-74-Mg is 1.89%, 5.89%, and 5.87%, respectively. A similar quantum

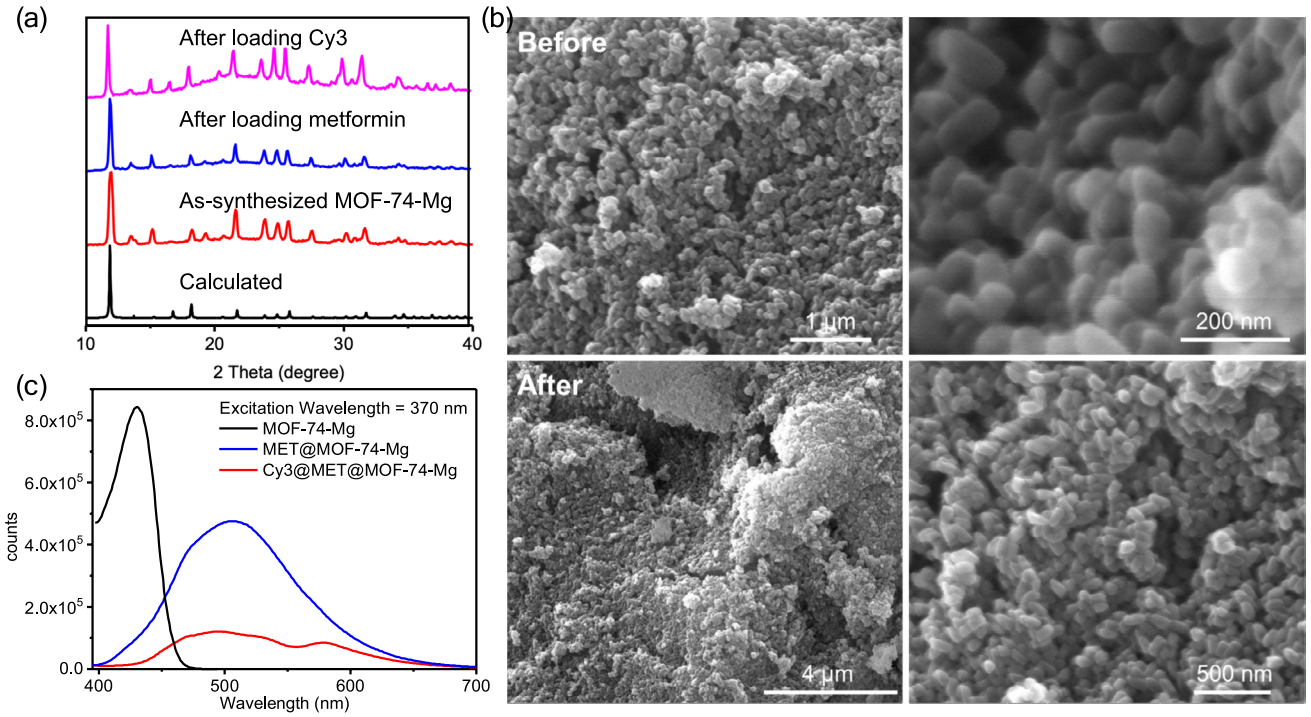

Fig. 2 Characterization of MOF-74-Mg. **a** PXRD patterns of nano-sized MOF-74-Mg. **b** SEM images of nano-sized MOF-74-Mg (average size: $135.3 \pm 15.6 \times 70.1 \pm 7.3$ nm) before and after Met loading. **c** Fluorescence spectra of MOF-74-Mg before and after Met and Cy3 loading

yield for Met-loaded MOF-74-Mg with and without Cy3 modification indicates a similar fluorescence signal by Cy3 dye and MOF-74-Mg and suggests that MOF-74-Mg alone can potentially provide fluorescence signals for biodetection.

3.2 High Met payload and sustained release of MOF-74-Mg

The LE and payload reflect the capacity of MOF-74-Mg to encapsulate Met. UV light absorbance spectra (Fig. 3a) depict the original Met solution and supernatant fluid after the Met-loaded MOF-74-Mg removal. By calculating from a standard curve, the amount of Met in the original solution and supernatant fluid is 300 mg and 170 mg, respectively. It reveals 130 mg of loaded Met and yields LE of 43.3% and payload of 10% wt/wt (Eqs. 1 and 2), higher than previous MOF reports [33, 34]. The drug release profile of Met-loaded MOF-74-Mg in DMEM for up to 16 h (Fig. 3b) indicated sustained Met release without burst. Approximately 90% of Met was released after 16 h in DMEM. The absence of an initial burst release suggests that most Met molecules are likely encapsulated within the pores of MOF-74-Mg, which is crucial for sustained and prolonged release over time.

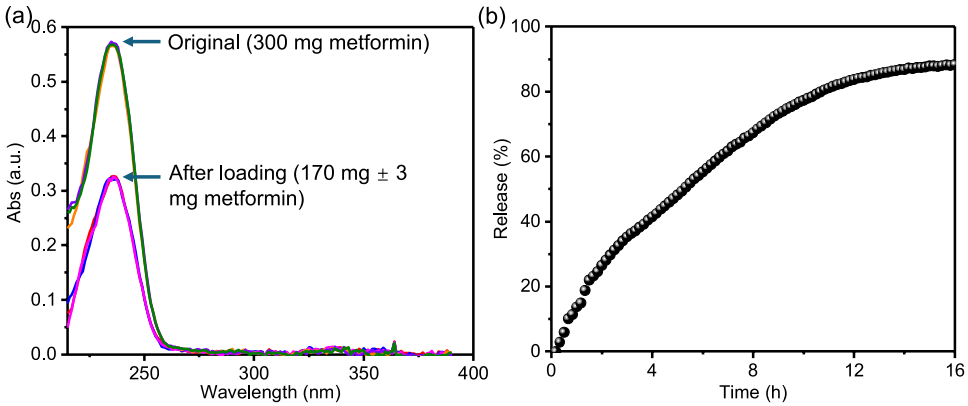

Fig. 3 **a** UV light absorbance spectra for Met loading into 1.3 g of MOF-74-Mg. **b** The Met release profile

3.3 MOF-74-Mg exhibited dose-dependent biocompatibility

To evaluate the biocompatibility of Met-loaded MOF-74-Mg, we performed the cell viability test on Neuro-2A cells treated with Met-loaded MOF-74-Mg at concentrations up to 30 mg/mL (Fig. 4a). At 5 mg/mL, cell viability remained above 90% for all the time points. However, viability decreased to 70% at 10 mg/mL and dropped below 10% at 20 and 30 mg/mL. The results suggested toxicity of Met-loaded MOF-74-Mg at the concentration of 10 mg/mL and above. Literature reported the observed cytotoxicity of MOF-74-Co at the concentration of 0.1 mg/mL [53]. Meanwhile, MIL-100 and ZIP-8 NPs showed IC50 (half maximal inhibitory concentration) of 0.7 and 0.025 mg/mL [54]. Compared to previously reported MOFs, our MOF-74-Mg NCs exhibited much lower cytotoxicity.

3.4 *Met-MOF affected the H_2O_2-induced cell viability loss*

To assess the impact of Met on H_2O_2-induced cell viability loss, Neuro-2A cells were first incubated with various H_2O_2

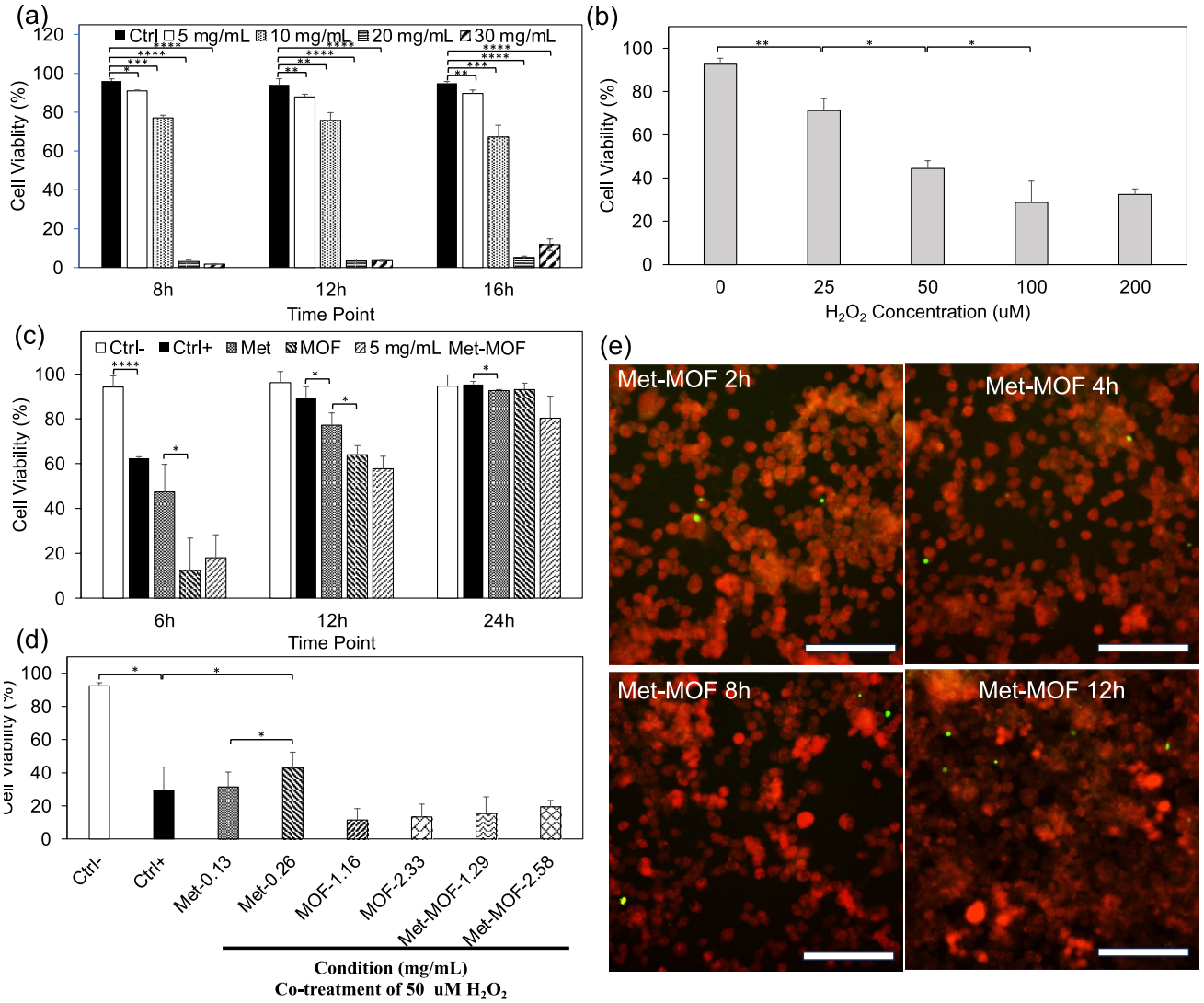

Fig. 4 In vitro evaluation of Met-MOF in neuro2A cells: **a** The biocompatibility study of MOF: cell viability results by flow cytometry at 8, 12, and 16 h for Met-loaded MOF-74-Mg at the concentration of 0, 5, 10, 20, and 30 mg/mL. **b–d** Impact of Met on cell viability loss induced by H_2O_2 in Neuro2A cells: **b** H_2O_2 induced cell viability loss. **c** Viability of Neuro2A cells treated with Met (0.45 mg/mL, which is equivalent to 3.49 mM), MOF (4.05 mg/mL), and Met-MOF (total concentration 4.5 mg/mL, with 0.45 mg/mL Met and 4.05 mg/mL MOF) at different time points, followed by treatment of 50 μM H_2O_2. **d** Viability of Neuro2A cells treated with Met (0.13 mg/mL and 0.26 mg/mL, which is equivalent to 1 mM and 2 mM), MOF (1.16 and 2.33 mg/mL), and Met-MOF (total concentration of 1.29 and 2.58 mg/mL), with the co-treatment of 50 μM H_2O_2. **e** Neuro-2A cells-MOF interaction at different time points by fluorescence microscopy. Scale bar = 150 μm. (*$p < 0.05$, **$p < 0.01$, ***$p < 0.001$, ****$p < 0.0001$)

concentrations for 24 h, with viability determined by flow cytometry (Fig. 4b). At 50 μM H_2O_2, a significant viability loss of over 50% was observed. Thus this H_2O_2 concentration was selected for Met evaluation. Cells were then treated with pure Met, pure MOF, and Met-MOF for 6, 12, and 24 h prior to H_2O_2 exposure at 50 μM for 24 h, with the no treatment groups (Ctrl-) and only H_2O_2 treated groups (Ctrl +) as controls. Flow cytometry results (Fig. 4c) showed that viability slightly decreased by 6 h of pretreatment with 3.49 mM Met compared to the Ctrl + group. Literature suggests that Met induces neuroprotection in PC-12 cells against H_2O_2-induced oxidative stress at concentrations below 0.5 mM, with reduced viability at 5 mM [55]. Moreover, its neuroprotection mechanism, involving antioxidant levels such as glutathione and catalase and the P13K/S6K pathway, is dose-dependent and effective below 2 mM. At high Met concentrations, the P13K/S6K pathway is suppressed, which possibly causes reduced viability. The reduced viability and apoptotic changes in cell morphology by 5 mM Met are also observed in the human T98G cell line [56]. However, the concentration dependence of Met on Neuro-2A cell viability remains unexplored in existing literature.

Additionally, it was observed that the 6 h of MOF pretreatment further reduced viability (Fig. 4c), possibly due to the increased vulnerability induced by H_2O_2 and the less tolerance to MOF at longer incubation time (6 + 24 h). This is consistent with the literature on the synergistic toxicity of H_2O_2 with other agents [57]. Met-MOF exhibited slightly higher viability than the MOF-only group, likely due to the neuroprotective effect of the 55% released Met at 6 h, which was 1.9 mM. The neuroprotection by this Met concentration is consistent with the findings in the literature [58].

When the cells were pretreated for longer durations (12 h and 24 h), viability gradually increased across all groups, possibly due to the higher cell density. Literature suggests cell-density dependence of H_2O_2-induced cytotoxicity: higher cell density led to higher viability [59], as each cell consumes fewer H_2O_2 molecules, leading to less toxicity. Met-MOF groups exhibited lower viability at longer pretreatment time (12 h and 24 h) than MOF alone, likely due to the over 85% Met release after 12 h, according to Met release kinetics. This resulted in Met concentrations higher than 3 mM, suppressing the PI3K/S6K pathway [55].

To test the dose-dependent neuroprotection of Met in Neuro-2A cells, we studied Met at lower concentrations (2 mM and 1 mM) and the equivalent concentrations of Met-MOF and MOF. Cells were co-treated with H_2O_2 and Met/MOF/Met-MOF simultaneously to maintain consistent cell density. Adding H_2O_2 induced over 60% viability loss in the Ctrl + group (Fig. 4d). Met at 2 mM (0.26 mg/mL) recovered viability by 13.5%. In contrast, Met at 1 mM did not show the same effect, confirming Met's dose-dependent neuroprotective function. Pure MOF induced further dose-dependent viability loss in the H_2O_2-treated group, likely due to previously mentioned synergistic toxicity [57]. In the Met-MOF group co-treated by H_2O_2, viability slightly recovered compared to pure MOF, attributed to Met's neuroprotective effect.

Employing fluorescence imaging, we verified the self-indicating ability of MOF-74-Mg in Neuro-2A cells. Figure 4e illustrates the Met-MOF in blue and cells in red after incubating cells with Met-MOF for varying durations. The results demonstrate our NC's excellent fluorescence signal for self-indicating and its interaction with Neuro-2A cells. Green fluorescent dots inside cells indicate MOF-74-Mg uptake. After longer incubation (12 h), more MOF-74-Mg were observed inside cells. Compared to other drug carriers requiring additional fluorescence tags [60], our NCs show inherent fluorescence, indicating their potential for accurately tracking biodistribution and understanding the NCs' delivery pathway.

3.5 IN administered Cy3-labeled Met-MOF incorporated into neurons and microglia cell bodies within different brain regions in 5xFAD mice

The immunofluorescence staining of brain tissue sections was performed to verify the effectiveness of IN delivery of Met-MOF to the brain and demonstrate the accumulation of Met-MOF in different neural cell types in various brain regions 45 min after injection. Investigation of Cy3 + structures in serial brain tissue sections processed for NeuN and Iba1 immunofluorescence using 1.5 μm thick optical Z-sections in a confocal microscope revealed widespread incorporation of IN-administered Met-MOF into neurons and microglia in the medial prefrontal cortex, hippocampal subfields (DG, CA1, and CA3), striatum, perirhinal cortex, and midbrain. The particles were incorporated into ~79–85% of neurons and 93–97% of microglia cells (Fig. 5a–f, i, j–o, r). 3D and orthogonal views of neurons (Fig. 5g, h) and microglia (Fig. 5p, q) confirmed the internalization of Met-MOF NCs into neurons and microglia. Incorporating Met-MOF in neurons suggests their potential to deliver neuroprotective agents to neurons directly. In addition, microglia are the primary immune cells in the CNS [27]. While microglia typically protect neurons by clearing harmful substances, activation can lead to neuronal damage and chronic neuroinflammation [27]. The incorporation of Met-MOF into microglia indicated their microglia-targeting ability without additional targeting ligands or peptides, which can potentially incorporate agents to inhibit toxic protein aggregation and modulate microglia-mediated inflammatory signaling cascades. In addition, literature reported the neuronal uptake

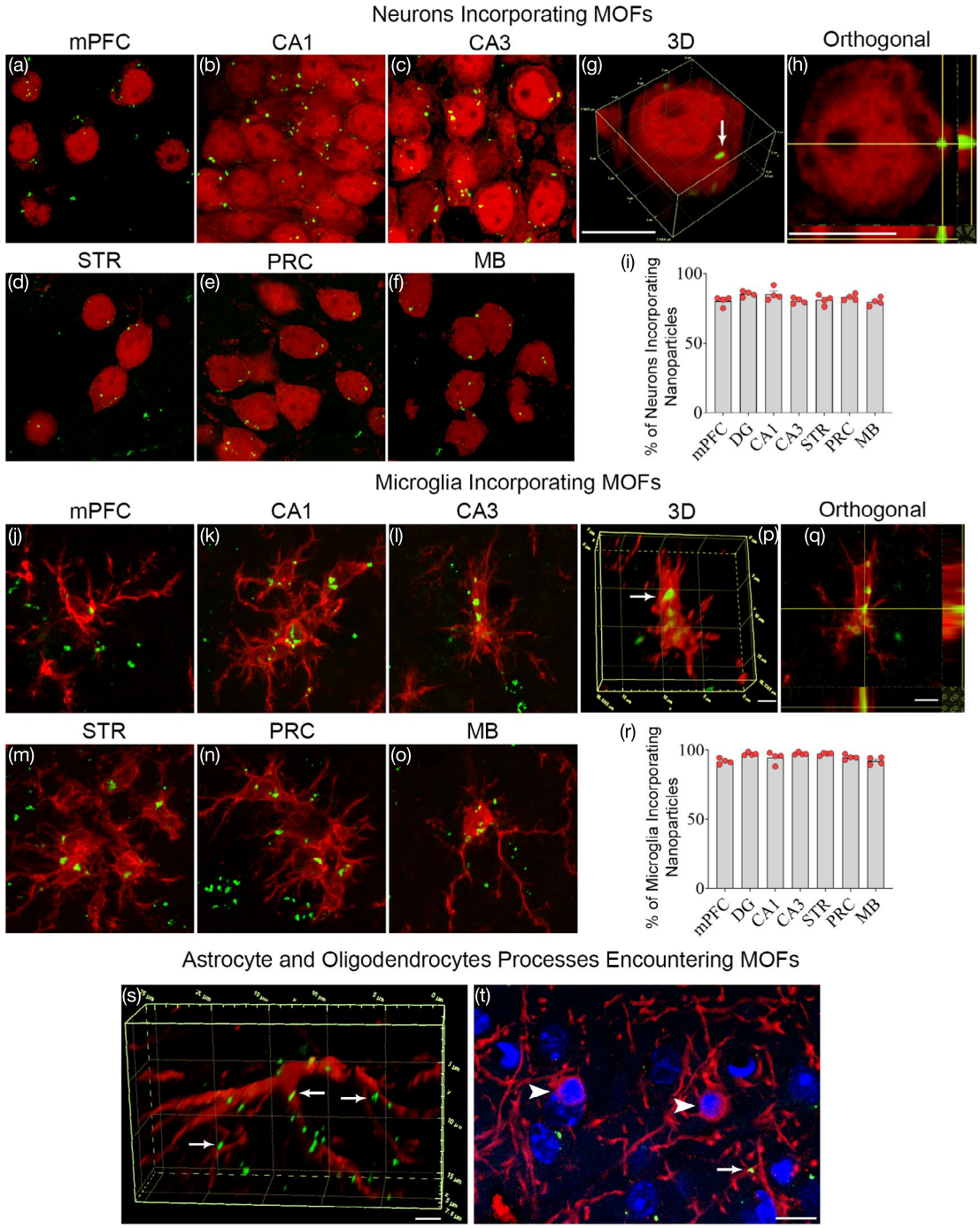

Fig. 5 Confocal fluorescence imaging of intranasally administered Met-loaded MOF-74-Mg NCs incorporated into different brain regions in AD mice. **a–f** The confocal images from the different regions of the brain showing the NeuN + neurons (in red) incorporating the Cy3-labeled Met-MOFs (in green/yellow) with the 3D image (**g**) of a neuron from CA3 subregion of the hippocampus containing the Met-MOF and the orthogonal view (**h**) of the same neuron from CA3 subregion. Graph (**i**) shows the percent number of neurons that incorporated the Met-MOFs in the different regions of the brain. **j–o** The IBA1 + microglia (in red) incorporating the Met-MOFs (in green/yellow) in the different regions of the brain with the 3D image (**p**) of the microglia from the CA3 subregion containing the Met-MOFs and the orthogonal view (**q**) of the same microglia with Met-MOFs. Graph (**r**) shows the percentage of microglia incorporating the Met-MOFs in the different regions of the brain. **s, t** The processes of GFAP + astrocytes (in red) and CNPase + oligodendrocytes (processes in red and nucleus in blue) that encounter the Met-MOFs (in green). mPFC, Medial Prefrontal Cortex; DG, Dentate Gyrus; CA1, Cornu ammonis 1 (subregion of hippocampus); STR, Striatum; PRC, Perirhinal Cortex; MB-Midbrain; Scale: Images are × 60 with the scale bar = 5 µm

ability of other NPs. Poly (lactic-co-glycolic acid) (PLGA) NPs exhibited a neuronal uptake rate of 6% at 4 h [61]. Silica NPs exhibited a time-dependent microglia uptake with a maximum 70% uptake at 1 h and a higher uptake rate at a longer time [62]. Compared to the literature results, our NCs have a much higher neuron and microglia incorporation rate at 45 min after administration.

3.6 IN administered Cy3-labeled Met-MOF encountered the processes of astrocytes and oligodendrocytes in the brain of 5xFAD mice

Probing of Met-MOF structures in representative brain tissue sections processed for GFAP and CNPase immunofluorescence using 1.5 µm thick Z-sections in a confocal microscope revealed the apposition of IN-administered Met-MOF into oligodendrocyte and astrocytic processes (Fig. 5s, t). The in vivo results showed how the Met-MOF is differentially delivered into neurons, microglia, astrocytes, and oligodendrocytes virtually in different brain regions. It could be observed that IN-administered Met-MOF interacted with the plasma membrane of processes and soma of astrocytes and oligodendrocytes across the brains of 5xFAD mice. However, instances of internalization of Met-MOF by these neural cells were significantly fewer compared to neurons and microglia, suggesting that the mechanism of Met-MOF transfer into astrocytes and oligodendrocytes differs from that into neurons and microglia within the brain.

3.7 MOF-74-Mg accumulated in different brain regions after IN delivery

To quantitatively assess brain distribution of MOF-74-Mg across different brain regions and time points, elemental analysis was conducted on Mg concentration in brain tissues at 8, 12, and 16 h post-IN delivery in wild-type mice. As shown in Fig. 6, for all the interested brain areas, brain concentration of MOF-74-Mg peaked at 8 h, gradually declining at 12 h and 16 h. The frontal cortex exhibited the highest accumulation for all the measured time points, while the striatum showed the lowest. According to the total collected tissue weight (about 233 mg, while total brain weight was about 416 mg), approximately 2 mg of MOF-74-Mg, comprising 9% of the injected dose, was found in the collected brain tissue. We did not measure the time points shorter than 8 h. Therefore, the peak time may be less than 8 h. Also, at high doses by IN delivery, NCs may not be able to fully enter the IN pathway, and a large portion of NPs may be restricted by the protective barriers that exist in the nasal mucosa from entering the IN pathway [63]. To further demonstrate the peak time and improve the brain accumulation of MOF-74-Mg NCs by IN delivery, future studies will explore the brain concentration of MOF-74-Mg at a shorter time, such as 45 min, 3 h, and 6 h, and lower doses. Previous literature found that the direct IN delivery of pure Met without using NCs did not improve the brain targeting of Met [64]. Notably, by oral administration, Met exhibited a maximum accumulation level of 13.5 nmol/g in rat brains at

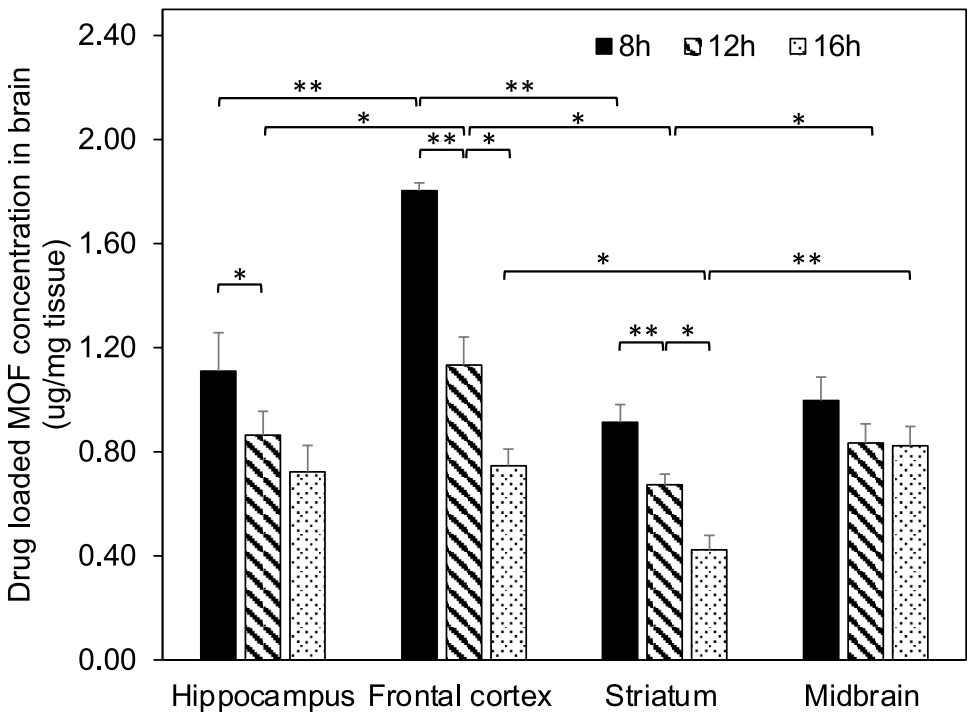

Fig. 6 Brain concentration of MOF-74-Mg by ICP-MS. (*$p < 0.05$; **$p < 0.01$)

6 h after administration, which is 2.2×10^{-3} µg/mg (approximately 0.02% of the dose at 150 mg/kg) [65]. The delivery percentage and the brain accumulation level are much lower than our results (9% and 0.48 µg/mg), even though their dosage is much higher than that in our case (76 mg/kg). Our results demonstrated a higher level of brain accumulation of Met (82 times the oral case's reference value) using MOF as NCs compared to oral administration and previous IN administration results. This work suggests an innovative way to enhance the brain accumulation of Met by using NC to promote the targeting of the brain via the nose-to-brain pathway. In the future, we will further optimize the MOF structure to enable a higher loading rate. For example, a crystal defect method will be employed to create a multi-level pore in MOF structure by replacing part of the metal source with Cl^- based metal source, resulting in the formation of MOF-74-Mg with defects in the crystal [66]. Alternatively, the MOF structure can be modified to enhance the drug loading rate by creating hollow spaces within the framework [67]. We also plan to explore drug-MOF interactions in greater detail, using techniques such as N_2 adsorption–desorption isotherms to assess the occupation of drugs within the pores quantitatively [68]. Additionally, machine learning algorithms can optimize the structure modification process to predict drug loading capacities more accurately [74]. Incorporating stimuli-responsive properties into MOF structure can enable controlled drug release [69, 70]. By integrating internal or external stimuli, such as light, heat, and pressure, the drug-release process can be regulated with more precision [71]. To enhance targeting capacities, MOF structures can be functionalized with targeting moieties, such as peptides or antibodies, that interact specifically with receptors located on the cell membranes [72]. Furthermore, MOF NCs can be coated with natural polymers such as gelatin [73] to minimize immune system elimination.

4 Conclusions

We have successfully synthesized porous and fluorescent MOF-74-Mg nanostructures as NCs of Met. SEM and XRD confirmed the formation of the structure. The NCs showed a high Met loading rate and a sustained Met release pattern for up to 16 h. The inherent fluorescence of MOF-74-Mg acted as a self-indicator without additional fluorescence dyes. Moreover, cell experiments confirmed the low toxicity of MOF-74-Mg at a concentration below 10 mg/mL. An in vivo study showed that IN administration delivered 9% of the Met-MOF into the mouse brain.

Moreover, Met-MOF accumulated notably in neurons and microglia across various brain regions including the medial prefrontal cortex, hippocampus, striatum, perirhinal cortex, and midbrain in 5xFAD mice. Met-MOF also interacted with astrocytes and oligodendrocytes, but internalization by these cells was less frequent than by neurons and microglia, indicating a differing transfer mechanism. The results revealed the high potential of multifunctional MOF-74-Mg as NCs with high drug loading rates, intrinsic fluorescence, and brain targeting ability via IN delivery. In the future, we will perform functional studies of Met-encapsulated MOF-74-Mg to explore their impact on cognitive recovery in AD mice.

Acknowledgements We would also like to acknowledge the Elemental Analysis Lab at the Chemistry Department of Texas A&M University for performing ICP-MS analysis in this study.

Author contribution M. Y., Z. H., L. N. M., R. S., A. K. S., and Y. W. conceived and designed the study. Z. H., Y. S., N. N., H. H., L. N. M., S. A., M. K., Y. Y., Y-C. H. and A. A. performed the experiments. M. Y., Z. H., Y. S., N. N., S. A., L. N. M., J-P. P., H-C. Z., A. K. S. and Y.W. analyzed the data and interpreted the results. M. Y., Z. H, and Y.W. wrote the paper. All authors discussed, revised, and commented on the manuscript writing.

Funding This work was kindly supported by the United States National Science Foundation (NSF) (CAREER Award # CMMI 1851635, Y.W. and GCR awards # ECCS 2021081 (Y.W. and R.S.) and the National Institutes of Health—National Institute on Aging (1RF1AG074256-01 to A.K.S.).

Data availability The datasets generated and/or analyzed during the current study are available from the corresponding author, M. Y., Y. W., and Z. H., upon reasonable request.

Declarations

Conflict of interest The authors declare no competing interests.

References

1. Ou Z, Kong X, Sun X, He X, Zhang L, Gong Z, Huang J, Xu B, Long D, Li J (2018) Metformin treatment prevents amyloid plaque deposition and memory impairment in APP/PS1 mice. Brain Behav Immun 69:351–363
2. Paudel YN, Angelopoulou E, Piperi C, Shaikh MF, Othman I (2020) Emerging neuroprotective effect of metformin in Parkinson's disease: a molecular crosstalk. Pharmacol Res 152:104593

3. Cho SY, Kim EW, Park SJ, Phillips BU, Jeong J, Kim H, Heath CJ, Kim D, Jang Y, López-Cruz L (2024) Reconsidering repurposing: long-term metformin treatment impairs cognition in Alzheimer's model mice. Transl Psychiatry 14:34
4. Foretz M, Guigas B, Viollet B (2023) Metformin: update on mechanisms of action and repurposing potential. Nat Rev Endocrinol 19:460–476
5. Mor DE, Sohrabi S, Kaletsky R, Keyes W, Tartici A, Kalia V, Miller GW, Murphy CT (2020) Metformin rescues Parkinson's disease phenotypes caused by hyperactive mitochondria. Proc Natl Acad Sci 117:26438–26447
6. Kodali M, Attaluri S, Madhu LN, Shuai B, Upadhya R, Gonzalez JJ, Rao X, Shetty AK (2021) Metformin treatment in late middle age improves cognitive function with alleviation of microglial activation and enhancement of autophagy in the hippocampus. Aging Cell 20:e13277
7. Guo X, Zhang B, Chen Y, Jia Z, Yuan X, Zhang L, Liu J, Liu Y (2024) Multifunctional mesoporous nanoselenium delivery of metformin breaks the vicious cycle of neuroinflammation and ROS, promotes microglia regulation and alleviates Alzheimer's disease. Colloids and Surfaces B: Biointerfaces 114300
8. Sanati M, Aminyavari S, Afshari AR, Sahebkar A (2022) Mechanistic insight into the role of metformin in Alzheimer's disease. Life Sci 120299
9. Luchsinger JA, Perez T, Chang H, Mehta P, Steffener J, Pradabhan G, Ichise M, Manly J, Devanand DP, Bagiella E (2016) Metformin in amnestic mild cognitive impairment: results of a pilot randomized placebo controlled clinical trial. J Alzheimer's Disease 51:501–514
10. McCreight LJ, Bailey CJ, Pearson ER (2016) Metformin and the gastrointestinal tract. Diabetologia 59:426–435
11. Lv W-s, Wen J-p, Li L, Sun R-x, Wang J, Xian Y-x, Cao C-x, Wang Y-l, Gao Y-y (2012) The effect of metformin on food intake and its potential role in hypothalamic regulation in obese diabetic rats. Brain Res 1444:11–19
12. Timmins P, Donahue S, Meeker J, Marathe P (2005) Steady-state pharmacokinetics of a novel extended-release metformin formulation. Clin Pharmacokinet 44:721–729
13. Chen M, Shu Y, Li Q, Kang Z, Liu T, Zhou H, Huang W, Zhang W (2023) Bacteroides ovatus accelerates metformin-induced vitamin B12 deficiency in type 2 diabetes patients by accumulating cobalamin. npj Biofilms Microbiomes 9:51
14. Wu D, Chen Q, Chen X, Han F, Chen Z, Wang Y (2023) The blood–brain barrier: structure, regulation, and drug delivery. Signal Transduct Target Ther 8:217
15. Mitragotri S, Burke PA, Langer R (2014) Overcoming the challenges in administering biopharmaceuticals: formulation and delivery strategies. Nat Rev Drug Discovery 13:655–672
16. Nguyen N, Yuan M, Hu H, Xiao Z, Fan T, Yan T-H, Li Y, Zhou HC, Pellois J-P, Wang Y (2024) Computational fluid-particle dynamic model guiding bioengineered magnetic nanomedicine for personalized brain-targeted drug delivery. Adv Compos Hybrid Mater 7:1–24
17. Chen J, Yuan M, Madison CA, Eitan S, Wang Y (2022) Blood-brain barrier crossing using magnetic stimulated nanoparticles. J Control Release 345:557–571
18. Hu H, Yuan M, Chen J, Fan T, Nguyen N, Madison CA, Yan T, Xiao Z, Li Y, Eitan S (2024) Pharmacokinetic modeling of solid and hollow gold-coated superparamagnetic iron oxide nanoparticles for brain-targeted therapeutics: prediction and experiment. Adv Compos Hybrid Mater 7:76
19. Henkin RI (2011) Intranasal delivery to the brain. Nature Biotechnol 29:480-
20. Hanson LR, Fine JM, Svitak AL, Faltesek KA (2013) Intranasal administration of CNS therapeutics to awake mice. JoVE J Visual Exp e4440
21. Lu Y, Wang JT-W, Li N, Zhu X, Li Y, Bansal S, Wang Y, Al-Jamal KT (2023) Intranasal administration of edaravone nanoparticles improves its stability and brain bioavailability. J Control Release 359:257–267
22. Mahajan HS, Mahajan MS, Nerkar PP, Agrawal A (2014) Nanoemulsion-based intranasal drug delivery system of saquinavir mesylate for brain targeting. Drug Delivery 21:148–154
23. Yadav S, Gattacceca F, Panicucci R, Amiji MM (2015) Comparative biodistribution and pharmacokinetic analysis of cyclosporine-A in the brain upon intranasal or intravenous administration in an oil-in-water nanoemulsion formulation. Mol Pharm 12:1523–1533
24. Lee MR, Scheidweiler KB, Diao XX, Akhlaghi F, Cummins A, Huestis MA, Leggio L, Averbeck BB (2018) Oxytocin by intranasal and intravenous routes reaches the cerebrospinal fluid in rhesus macaques: determination using a novel oxytocin assay. Mol Psychiatry 23:115–122
25. Mitchell MJ, Billingsley MM, Haley RM, Wechsler ME, Peppas NA, Langer R (2021) Engineering precision nanoparticles for drug delivery. Nat Rev Drug Discovery 20:101–124
26. Koirala P, Shalash AO, Chen S-PR, Faruck MO, Wang J, Hussein WM, Khalil ZG, Capon RJ, Monteiro MJ, Toth I (2024) Polymeric nanoparticles as oral and intranasal peptide vaccine delivery systems: the role of shape and conjugation. Vaccines 12:198
27. Zhao N, Francis NL, Calvelli HR, Moghe PV (2020) Microglia-targeting nanotherapeutics for neurodegenerative diseases. APL Bioeng 4
28. Peruzzotti-Jametti L, Willis CM, Krzak G, Hamel R, Pirvan L, Ionescu RB, Reisz JA, Prag HA, Garcia-Segura ME, Wu V (2024) Mitochondrial complex I activity in microglia sustains neuroinflammation. Nature 628:195–203
29. Khezri MR, Yousefi K, Mahboubi N, Hodaei D, Ghasemnejad-Berenji M (2022) Metformin in Alzheimer's disease: an overview of potential mechanisms, preclinical and clinical findings. Biochem Pharmacol 197:114945
30. Bag PP, Singh GP, Singha S, Roymahapatra G (2020) Synthesis of metal-organic frameworks (MOFs) and their biological, catalytic and energetic application: a mini review. Eng Sci 13:1–10
31. Dai L, Yao M, Fu Z, Li X, Zheng X, Meng S, Yuan Z, Cai K, Yang H, Zhao Y (2022) Multifunctional metal-organic framework-based nanoreactor for starvation/oxidation improved indoleamine 2, 3-dioxygenase-blockade tumor immunotherapy. Nat Commun 13:2688
32. Zhou H-C, Long JR, Yaghi OM (2012) Introduction to metal–organic frameworks. ACS Publications, Chemical reviews, pp 673–674
33. Vahed TA, Naimi-Jamal MR, Panahi L (2019) Alginate-coated ZIF-8 metal-organic framework as a green and bioactive platform for controlled drug release. J Drug Del Sci Technol 49:570–576
34. Vahed TA, Naimi-Jamal MR, Panahi L (2018) (Fe) MIL-100-Met@ alginate: a hybrid polymer–MOF for enhancement of metformin's bioavailability and pH-controlled release. New J Chem 42:11137–11146
35. Singh AV, Vyas V, Montani E, Cartelli D, Parazzoli D, Oldani A, Zeri G, Orioli E, Gemmati D, Zamboni P (2012) Investigation of in vitro cytotoxicity of the redox state of ionic iron in neuroblastoma cells. J Neurosci Rural Practice 3:301–310
36. Moezzi SMI, Javadi P, Mozafari N, Ashrafi H, Azadi A (2023) Metformin-loaded nanoerythrosomes: an erythrocyte-based drug delivery system as a therapeutic tool for glioma. Heliyon
37. Hafeez A-E, Sara I, Eleraky NE, Hafez E, Abouelmagd SA (2022) Design and optimization of metformin hydrophobic ion pairs for efficient encapsulation in polymeric drug carriers. Sci Rep 12:1–14
38. Deng H, Grunder S, Cordova KE, Valente C, Furukawa H, Hmadeh M, Gándara F, Whalley AC, Liu Z, Asahina S (2012) Large-pore apertures in a series of metal-organic frameworks. Science 336:1018–23
39. Fu Y, Yao Y, Forse AC, Li J, Mochizuki K, Long JR, Reimer JA, De Paëpe G, Kong X (2023) Solvent-derived defects suppress adsorption in MOF-74. Nat Commun 14:2386
40. Pederneira N, Newport K, Lawson S, Rownaghi AA, Rezaei F (2023) Drug delivery on Mg-MOF-74: the effect of drug solubility on pharmacokinetics. ACS Appl Bio Mater 6:2477–2486

41. Hashimoto T, Nishi K, Nagasao J, Tsuji S, Oyanagi K (2008) Magnesium exerts both preventive and ameliorating effects in an in vitro rat Parkinson disease model involving 1-methyl-4-phenylpyridinium (MPP+) toxicity in dopaminergic neurons. Brain Res 1197:143–151
42. Isaev NK, Stelmashook EV, Genrikhs EE (2020) Role of zinc and copper ions in the pathogenetic mechanisms of traumatic brain injury and Alzheimer's disease. Rev Neurosci 31:233–243
43. Yan X, Yang Q, Fang X, Xiong P, Liu S, Cao Z, Liao C, Liu S, Jiang G (2021) Co (ii)-based metal–organic framework induces apoptosis through activating the HIF-1α/BNIP3 signaling pathway in microglial cells. Environ Sci Nano 8:2866–2882
44. Han Z, Wang K, Min H, Xu J, Shi W, Cheng P (2022) Bifunctionalized metal–organic frameworks for pore-size-dependent enantioselective sensing. Angew Chem 134:e202204066
45. Zhang Z, Zhong T, Wang G (2022) Zn-MOF74 as a "turn-on" fluorescent chemosensor for recognition and detection of water in acetone and Al3+ in ethanol with high selectivity and sensitivity. J Photochem Photobiol, A 431:114052
46. Qiang H, Xia M, Wang F, Lei W, Lu X, Ni Y (2021) The highly specific detection and mechanism of Cu-MOF-74 fluorescent probe to amino trimethylene phosphonic acid: experimental study and theoretical calculation of quantum chemistry. J Mol Liq 341:117442
47. Belyaeva EA (2022) Role of mitochondrial respiratory chain in neurotoxic action of heavy metals: comparison of Cd2+, Hg2+ and Cu2+. Cut Edge Res Biol 2:144–174
48. Díaz-García M, Mayoral A, Diaz I, Sanchez-Sanchez M (2014) Nanoscaled M-MOF-74 materials prepared at room temperature. Cryst Growth Des 14:2479–2487
49. Kodali M, Castro OW, Kim D-K, Thomas A, Shuai B, Attaluri S, Upadhya R, Gitai D, Madhu LN, Prockop DJ (2019) Intranasally administered human MSC-derived extracellular vesicles pervasively incorporate into neurons and microglia in both intact and status epilepticus injured forebrain. Int J Mol Sci 21:181
50. Attaluri S, Jaimes Gonzalez J, Kirmani M, Vogel AD, Upadhya R, Kodali M, Madhu LN, Rao S, Shuai B, Babu RS (2023) Intranasally administered extracellular vesicles from human induced pluripotent stem cell-derived neural stem cells quickly incorporate into neurons and microglia in 5xFAD mice. Front Aging Neurosci 15:1200445
51. Huang X, Teng X, Chen D, Tang F, He J (2010) The effect of the shape of mesoporous silica nanoparticles on cellular uptake and cell function. Biomaterials 31:438–448
52. Lee C, Hwang HS, Lee S, Kim B, Kim JO, Oh KT, Lee ES, Choi HG, Youn YS (2017) Rabies virus-inspired silica-coated gold nanorods as a photothermal therapeutic platform for treating brain tumors. Adv Mater 29:1605563
53. Lan S, Zhang J, Li X, Pan L, Li J, Wu X, Yang S-T (2022) Low toxicity of metal-organic framework MOF-74 (Co) nano-particles in vitro and in vivo. Nanomaterials 12:3398
54. Tamames-Tabar C, Cunha D, Imbuluzqueta E, Ragon F, Serre C, Blanco-Prieto MJ, Horcajada P (2014) Cytotoxicity of nanoscaled metal–organic frameworks. J Mater Chem B 2:262–271
55. Khallaghi B, Safarian F, Nasoohi S, Ahmadiani A, Dargahi L (2016) Metformin-induced protection against oxidative stress is associated with AKT/mTOR restoration in PC12 cells. Life Sci 148:286–292
56. Ucbek A, Özünal ZG, Uzun Ö, Gepdİremen A (2014) Effect of metformin on the human T98G glioblastoma multiforme cell line. Exp Ther Med 7:1285–1290
57. Mahaseth T, Kuzminov A (2017) Potentiation of hydrogen peroxide toxicity: from catalase inhibition to stable DNA-iron complexes. Mut Res/Rev Mut Res 773:274–281
58. Zhao X, Zeng Z, Gaur U, Fang J, Peng T, Li S, Zheng W (2019) Metformin protects PC12 cells and hippocampal neurons from H2O 2-induced oxidative damage through activation of AMPK pathway. J Cell Physiol 234:16619–16629
59. Gülden M, Jess A, Kammann J, Maser E, Seibert H (2010) Cytotoxic potency of H2O2 in cell cultures: impact of cell concentration and exposure time. Free Radical Biol Med 49:1298–1305
60. Alijani H, Noori A, Faridi N, Bathaie SZ, Mousavi MF (2020) Aptamer-functionalized Fe3O4@ MOF nanocarrier for targeted drug delivery and fluorescence imaging of the triple-negative MDA-MB-231 breast cancer cells. J Solid State Chem 292:121680
61. Li R, Huang Y, Chen L, Zhou H, Zhang M, Chang L, Shen H, Zhou M, Su P, Zhu D (2019) Targeted delivery of intranasally administered nanoparticles-mediated neuroprotective peptide NR2B9c to brain and neuron for treatment of ischemic stroke. Nanom Nanotechnol Biol Med 18:380–390
62. Ducray AD, Stojiljkovic A, Möller A, Stoffel MH, Widmer H-R, Frenz M, Mevissen M (2017) Uptake of silica nanoparticles in the brain and effects on neuronal differentiation using different in vitro models. Nanomedicine: Nanotechnology. Biol Med 13:1195–1204
63. Dhuria SV, Hanson LR, Frey Ii WH (2010) Intranasal delivery to the central nervous system: mechanisms and experimental considerations. J Pharm Sci 99:1654–1673
64. Iwasaki S, Yamamoto S, Sano N, Tohyama K, Kosugi Y, Furuta A, Hamada T, Igari T, Fujioka Y, Hirabayashi H (2019) Direct drug delivery of low-permeable compounds to the central nervous system via intranasal administration in rats and monkeys. Pharm Res 36:1–14
65. Łabuzek K, Suchy D, Gabryel B, Bielecka A, Liber S, Okopień B (2010) Quantification of metformin by the HPLC method in brain regions, cerebrospinal fluid and plasma of rats treated with lipopolysaccharide. Pharmacol Rep 62:956–965
66. An H, Tian W, Lu X, Yuan H, Yang L, Zhang H, Shen H, Bai H (2023) Boosting the CO2 adsorption performance by defect-rich hierarchical porous Mg-MOF-74. Chem Eng J 469:144052
67. Gao X, Hai X, Baigude H, Guan W, Liu Z (2016) Fabrication of functional hollow microspheres constructed from MOF shells: promising drug delivery systems with high loading capacity and targeted transport. Sci Rep 6:37705
68. Arabbaghi EK, Mokhtari J, Naimi-Jamal MR, Khosravi A (2021) Zn-MOF: an efficient drug delivery platform for the encapsulation and releasing of Imatinib Mesylate. J Porous Mater 28:641–649
69. Rahaman SJ, Samanta A, Mir MH, Dutta B (2022) Metal-organic frameworks (MOFs): a promising candidate for stimuli-responsive drug delivery. ES Mater Manuf 19:792
70. He S, Wu L, Li X, Sun H, Xiong T, Liu J, Huang C, Xu H, Sun H, Chen W (2021) Metal-organic frameworks for advanced drug delivery. Acta Pharmaceutica Sinica B 11:2362–2395
71. Han Z, Yuan M, Nguyen N, Zhou H-C, Hubbard JE Jr, Wang Y (2024) Brain-specific targeted delivery of therapeutic agents using metal–organic framework-based nanomedicine. Coord Chem Rev 514:215926
72. Khafaga DSR, El-Morsy MT, Faried H, Diab AH, Shehab S, Saleh AM, Ali GAM (2024) Metal–organic frameworks in drug delivery: engineering versatile platforms for therapeutic applications. RSC Adv 14:30201–30229
73. Moharramnejad M, Ehsani A, Shahi M, Gharanli S, Saremi H, Malekshah RE, Basmenj ZS, Salmani S, Mohammadi M (2023) MOF as nanoscale drug delivery devices: synthesis and recent progress in biomedical applications. J Drug Del Sci Technol 81:104285
74. Wei K, Shi Y, Tan X, Shalash M, Ren R, Faheim AA, Jia C, Huang R, Sheng Y, Guo Z (2024) Recent development of metal-organic frameworks and their composites in electromagnetic wave absorption and shielding applications. Adv Coll Interf Sci 103271
75. He L (2020) Metformin and systemic metabolism. Trends Pharmacol Sci 41:868–881
76. Gumieniczek A, Berecka-Rycerz A, Mroczek T, Wojtanowski K (2019) Determination of chemical stability of two oral antidiabetics, metformin and repaglinide in the solid state and solutions using LC-UV, LC-MS, and FT-IR methods. Molecules 24:4430